



Flow-induced vibration analysis of elastic propellers in a cyclic inflow: An experimental and numerical study

Jin Tian^{a,b,*}, Zhenguo Zhang^{a,b}, Zhen Ni^{a,b}, Hongxing Hua^{a,b}

^a Institute of vibration, shock and noise, Shanghai Jiao Tong University, 800 Dongchuan Road, Shanghai 200240, PR China

^b State Key Laboratory of Mechanical System and Vibration, Shanghai Jiao Tong University, 800 Dongchuan Road, Shanghai 200240, PR China



ARTICLE INFO

Article history:

Received 16 August 2016

Received in revised form 24 March 2017

Accepted 24 March 2017

Available online 2 April 2017

Keywords:

Flow-induced vibration

Marine propeller

Acceleration measurements

Pressure fluctuations

Large eddy simulation

ABSTRACT

In this paper, the flow-induced vibrations of marine propellers in cyclic inflows are investigated both experimentally and numerically. A Laser-Doppler velocimetry (LDV) system is used to measure the axial flow velocity distributions produced by the seven-cycle wake screen in the water tunnel. A customized underwater slip ring and a single axis accelerometer sealed by silicon sealant are employed to measure the acceleration responses of rotating propeller blade. Numerical simulations of pressure fluctuations on the blades are performed using large eddy simulation (LES), while the forced vibrations of the propeller blades are obtained by a combined finite element and boundary element method. Experimental and numerical results are presented for two model propellers with the same geometries and different flexible properties, which show that the propeller blade vibrates at a frequency which is seven times as large as the axial passing frequency (APF) in the seven-cycle inflow. Moreover, the propeller blades are observed to resonance when the 7 APF excitation frequency is equal to the fundamental frequency of the propellers. The results indicate that both the inflow feature and the modal characteristic of blades contribute to flow-induced vibrations of elastic propellers.

© 2017 Elsevier Ltd. All rights reserved.

1. Introduction

In recent years, flow-induced propeller vibration has become an active area of research. This vibration can be caused by vortex shedding, turbulence or inflow distortion. The inflow non-uniformities are the main reason in many situations. For example, the propeller was forced to vibrate at a particular frequency when operating in the non-uniform inflow produced by the rudder. This vibration is harmful to both the propeller and the hull, for it produces strong hydrodynamic pressure fluctuations and unsteady thrust, which generate unwanted underwater flow noise and structure-borne noise [1].

Brooks [2] firstly carried out the deep research of the vibrations of a marine propeller operating in a nonuniform inflow. The research was focused on the effect of blade vibration on the unsteady forces developed by different marine propellers. Three-cycle and four-cycle wake screen were used to generate the cyclic inflows. The experimental results showed that the unsteady thrust and torque, presented as a function of excitation frequency, was

related to the elastic properties of the propellers. The flexible propeller demonstrated large force amplification near its resonance frequency while the rigid one did not. The study also showed that blade vibration can significantly reduce the unsteady forces transmitted to the propeller shaft over a certain range of excitation frequencies. A numerical method was developed to calculate the unsteady forces which were in general agreement with the experimental measurements.

The vibration of the propeller blade plays an important role in the vibration and noise control problem. Recently, fiber Bragg grating (FBG) based sensor technique has been widely used to measure the blade vibration when the propeller is operating in water. Javdani et al. [3] carried out an experimental study on a full-scale marine propeller to investigate the vibration behavior in air and water. In their study, a fiber Bragg grating based sensor network system was designed to obtain the vibration-induced strain with minimum influence to the characteristics of the blades. The results showed that the advanced optically-based experimental techniques can be used to investigate the vibration of actual multiple blade propellers of different types and sizes. However, the limitation of this research was that the propeller was not able to rotate in the tank. Seaver et al. [4] performed the research of the strain measurements of the propeller blades when rotating in a four-cycle inflow using FBGs embedded in the propeller blades.

* Corresponding author at: Institute of vibration, shock and noise, Shanghai Jiao Tong University, 800 Dongchuan Road, Shanghai 200240, PR China.

E-mail address: tianjinsjtu@sjtu.edu.cn (J. Tian).

The results showed the dynamic strain of the blade depended on the position of the blade in the four-cycle inflow. The dynamic response of the blade was found to have significant deviations from the measured flow velocities corresponding to the sensor locations, which illustrated the complex interplay of fluid and structural dynamics experienced by the propeller in the cyclic inflows. Nevertheless, the effect of the propeller's flexible property was not taken into account in this research.

Some researchers tended to use particle image velocimetry (PIV) or laser Doppler vibrometry (LDV) techniques to measure the blade vibration for these non-contact methods have no effect on the propeller blades [5–7]. Gwaghavanhu et al. [6] used photogrammetry and tracking laser Doppler vibrometry methods to investigate the rotating blade vibration. Mikrut et al. [7] used a commercial particle image velocimetry system to measure the blade vibration of a high-speed axial compressor. The results showed that when the compressor was operated at design air-mass flow rate, low amplitude vibrations in first bending and first torsion were discovered. The vibration amplitude for first bending and first torsion was found to triple when the compressor was operated at low air mass-flow rate, which corresponded to deep stall.

Numerical studies were also carried out on the flow-induced vibration problem. Lin et al. [8] performed the numerical analysis of underwater free vibration of a composite propeller blade. Rotational effects and added mass were considered using finite element method. The results showed that the natural frequency of the blade in water was much lower than in air, while the mode shapes of the blade in air were almost the same as that in water. Computational fluid dynamics (CFD) is a powerful method to study the flow-induced vibration problem. Ducoin et al. [9] investigated the hydroelastic response and stability of a flexible hydrofoil in viscous flow. They coupled the CFD solver CFX and a simple two-degrees-of-freedom (2-DOF) system to calculate the flow-induced response of the hydrofoil. The results showed that the viscous effects may lead to stall, buffeting, flutter, or resonance at high angles of attack due to periodic shedding of large-scale vortices. Wei et al. [10] performed a numerical study of the unsteady excitations from a 5-bladed propeller operating in the wake of a fully appended model submarine. Their research focused on the unsteady hydrodynamics of the propeller blades and acoustic response of the submarine hull due to the propeller excitations. The results showed that the unsteady forces due to the nonuniform wake played an important role in the submarine's underwater noise.

However, few researchers were able to carry out the comprehensive study of the flow-induced vibration problem of a propeller operating in a cyclic inflow. The present paper aims to investigate the vibration response of marine propellers in cyclic inflows, especially near the propeller's fundamental frequency. The experimental tests were performed in a water tunnel using two model propellers which have the same geometries but different flexible properties. Measured acceleration spectra were presented and discussed. Numerical simulations were carried out using CFD and a combined finite element and boundary element method. The pressure fluctuations induced by the seven-cycle inflow were analyzed. Furthermore, the effect of the propellers' elastic properties on the vibration response was studied.

2. Experimental set-up and techniques

The experiments were conducted in the water tunnel located at Shanghai Jiao Tong University. The tunnel test section is 0.7 m square by 10.6 m long in which the operating velocity range is 0–5 m/s. Fig. 1 shows the overall concept of the test rig in the water tunnel, which includes the model propeller, the shaft system, the wake screen and the slip ring. The shaft system is driven by a DC

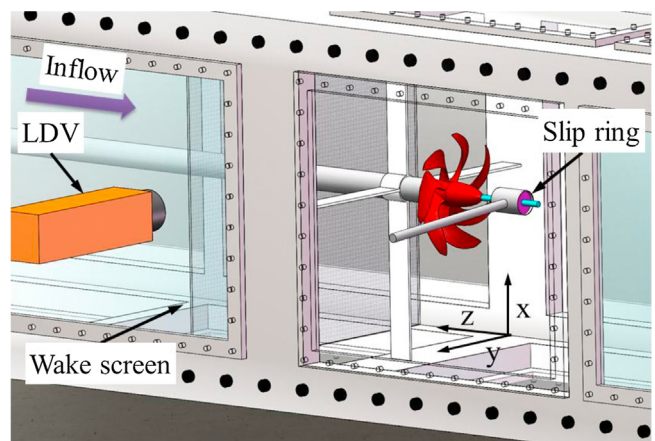


Fig. 1. The overall concept of the test rig in the water tunnel.

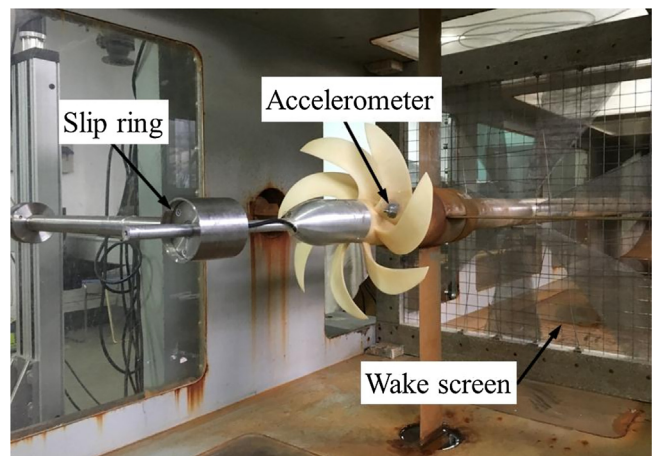


Fig. 2. Photograph of the slip ring, the accelerometer and the wake screen.

motor, which allows a maximum rotational speed of 1000 rpm. Two model propellers, which have the same geometries but made of different materials, were used in the tests. One propeller was made of flexible plastic with a fundamental frequency within the operating range of the test facility. The other propeller was made of bronze, with a fundamental frequency far beyond the operating range. Seven-cycle wake screen was used to generate the cyclic inflow.

2.1. Model propellers and the vibration data acquisition system

The propeller geometries consisted of 7 highly skewed blades which have a diameter of 250 mm. The detailed dimension of the propeller geometry is listed in Table 1. In Table 1, r is the radial location and R is the outer radius of the blades and in this work $R = 125$ mm. Table 2 shows the material properties of the two propellers.

A single axis accelerometer (Kistler type 8640) sealed by silicon sealant was mounted at $0.3R$ on the pressure side of the blade to measure the vibration response as shown in Fig. 2. This light weight accelerometer has a mass of 3.5 g and a sensitivity of 1000 mv/g.

The fundamental frequencies of each propeller in air and water were obtained by analyzing the measured frequency response functions. Five accelerometers were mounted on the shaft system as shown in Fig. 3. A series of excitations were applied on the propellers and the frequency response functions were measured to identify the propellers' fundamental frequencies in air and water.

Table 1
Geometry of the model propeller.

r\R	R (mm)	Pitch (mm)	Chord length (mm)	Thickness (mm)	Rake (mm)	Skew (degree)
0.2	125	357.875	45.25	11.925	0.1356	0.1078
0.3	125	353.1	49.975	10.225	-1.0877	-1.1855
0.4	125	351.1	53.8	8.9	-3.0948	3.9544
0.5	125	342.875	56.8	7.875	-5.5248	13.269
0.6	125	325.575	59.05	7	-5.4232	23.282
0.7	125	293.85	60.05	6.125	-2.2044	32.64
0.8	125	243.6	57.375	5	2.9036	41.052
0.9	125	179.625	45.75	3.375	9.3815	50.495
0.95	125	142.775	33.125	2.325	13.135	55.999
0.975	125	123.075	25.925	1.725	15.167	58.734
1	125	102.5	18.75	1.125	17.231	61.364

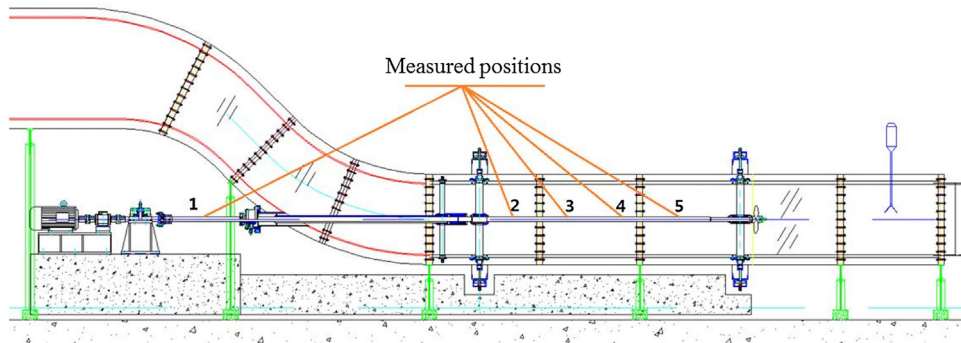


Fig. 3. Measured positions in the modal tests.

Table 2
Material properties of the model propellers.

	Density (kg/m ³)	Young's modulus (GPa)	Poisson ratio
Bronze propeller	8230	103	0.3
Plastic propeller	1200	1.5	0.31

A customized underwater slip ring as shown in Fig. 2 was used to transmit vibration signals from the rotating blade to the LMS SCADAS data acquisition System. LMS Test.Lab Spectral Testing was used to record and analyze the vibration signals during the testing.

2.2. Wake screen and LDV system

As the rotational speed of the propeller has a limitation of 1000 rpm, the maximum axis passing frequency (APF) is 16.7 Hz. In order to excite the resonance of the plastic propeller, seven-cycle wake screen was designed to generate the seven-cycle inflow. The location of the wake screen is 400 mm upstream of the propeller plane. This kind of wire mesh screen was an extension of that used in Jessup's [11] tests. The wake screen consisted of a coarse base screen (25 mm × 25 mm mesh size) which was soldered on to a steel frame and sections of dense screen (2 mm × 2 mm mesh size) which were overlapped over the coarse base screen. Several overlays were used to create a more sinusoidal wake pattern as shown in Fig. 2. Fig. 4 shows the schematic for the seven-cycle wake screen.

An ILA laser doppler velocimetry system located 100 mm downstream of the wake screen plane as shown in Fig. 1 was employed to measure the axial velocity distributions produced by the wake screen. The LDV system consists of a 2D probe, a 900 mm 3D traverse and a controller. There are two Nd:YAG lasers in the probe, which have a wavelength of 532 and 561 nm respectively. The lasers have a maximum power of 200 mW. The traversing system has a traverse resolution of 0.01 mm and is able to perform completely automated velocity measurements. An ultrasonic flowmeter was

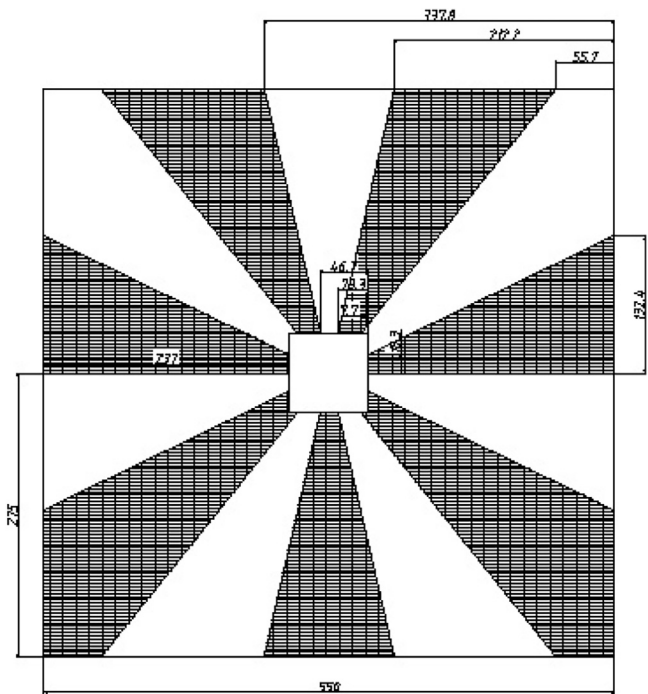


Fig. 4. The schematic of the seven-cycle wake screen.

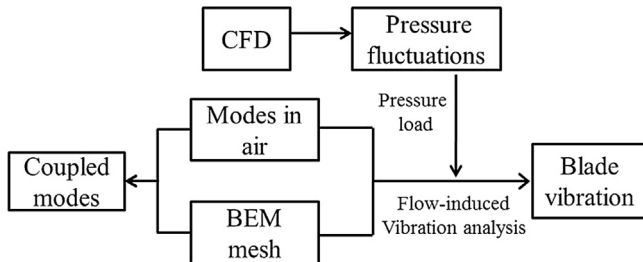
mounted 2000 mm downstream of the propeller plane to measure the tunnel speed U .

The LDV measurements were performed with the propeller operating behind the seven-cycle wake screen, at 0.1R and 8° increments from 0.2R to R and 0° to 360°, respectively. This series of measurements contained 414 measurement points in total. For each point, it required approximately 15 s to complete the mea-

Table 3

Test cases.

Advance ratio	Shaft rotational speed (r/min)
0	90, 120, 240, 360, 480, 600
0.31	90, 120, 240, 360, 480, 600, 626, 646, 666, 686, 700, 714, 728, 742, 756, 770

**Fig. 5.** Flow chart diagram of the numerical simulations.

surement. These measurements can be conducted automatically with the traversing system and control software.

2.3. Test cases

In order to compare the vibrations of the propeller in similar load condition, the experiments were expected to be performed at the same advance ratio. However, with the propeller operating behind the wake screen, there is no direct method to measure the freestream velocity V_a . This means there is no direct way for determining the advance ratio taken here as

$$J = \frac{V_a}{nD} \quad (1)$$

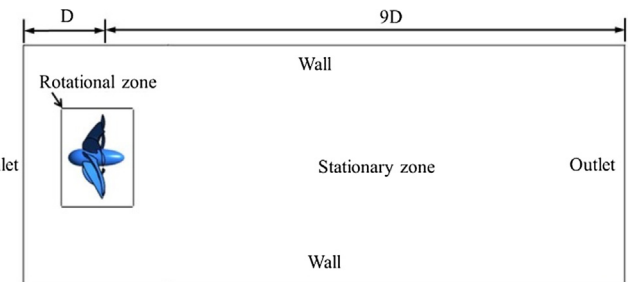
where V_a is the freestream velocity, n is the propeller's rotational speed in rotations per second, D is propeller's diameter.

In the present experiments, the measured tunnel velocity U was considered as the freestream velocity and used to calculate the advance ratio. **Table 3** lists the test cases for the two model propellers in the water tunnel. Initially, measurements were carried out at $J=0$. The purpose of these tests was to study the vibration of the propeller-shaft system. After these initial tests, measurements were conducted with $J=0.31$ and a series of shaft rotational speeds.

LMS Test.Lab Spectral Testing was used to record and analyze the signals. The bandwidth, frequency resolution and the number of averages was 1024 Hz, 0.25 Hz, 5 respectively in the tests. The Hanning window was used for the autopower spectrum calculations.

3. Numerical simulations

The numerical simulations were carried out with the following four steps: (i) the blade pressure fluctuations were calculated using the commercial CFD solver ANSYS-CFX (version 15.0); (ii) the natural modes of the propeller blade in vacuo were calculated using finite element method; (iii) the coupled modes were obtained using LMS Virtual.Lab; and (iv) the flow-induced vibration was calculated using LMS Virtual.Lab. In the flow-induced vibration analysis, the pressure fluctuations obtained in step (i) were considered as the load applied on the blade. A flow chart diagram outlining the various steps of the numerical procedure is shown in **Fig. 5**. Further details on the individual steps in the numerical simulations are given in what follows.

**Fig. 6.** Dimensions of the computational domain.

3.1. CFD model

In order to obtain the accurate pressure fluctuations of the propeller blades, large eddy simulation (LES) was used to resolve the flow field around the propeller. The filter function G is defined and a flow variable ϕ is filtered as [12]:

$$G(x, x') = \begin{cases} 1/V & x' \in v \\ 0 & x' \in \text{otherwise} \end{cases} \quad (2)$$

$$\bar{\phi}(x) = \int_v \phi(x') G(x, x') dx' \quad x' \in v \quad (3)$$

where V is the volume of a computational cell v . The governing equations for LES are derived by filtering the time-dependent incompressible Navier-Stokes equations as,

$$\frac{\partial \rho}{\partial t} + \frac{\partial}{\partial x_i} (\rho \bar{u}_i) = 0 \quad (4)$$

$$\frac{\partial}{\partial t} (\rho \bar{u}_i) + \frac{\partial}{\partial x_j} (\rho \bar{u}_i \bar{u}_j) = \frac{\partial}{\partial x_j} (\sigma_{ij}) - \frac{\partial \bar{p}}{\partial x_i} - \frac{\partial \tau_{ij}}{\partial x_j} \quad (5)$$

where ρ is the density, \bar{p} is the pressure, \bar{u}_i is the velocity component in the i^{th} direction after filtering. σ_{ij} is the stress tensor due to the molecular viscosity, $\tau_{ij} = \rho \bar{u}_i \bar{u}_j - \bar{\rho} \bar{u}_i \bar{u}_j$ is the subgrid-scale (SGS) stress. The approximate governing equations are obtained by modeling the SGS stress tensor using different models. In the present simulations using CFX, the Smagorinsky model was used for the calculations. The vibration of the blade was not taken into account in the LES simulations.

A cylinder computational domain which contained a rotational zone and a stationary zone was used to resolve the flow field of the propeller rotating through the non-uniform inflow. **Fig. 6** shows the dimensions of the computational domain. The cylinder has a diameter of $3D$ and a length of $10D$. The distance from the inlet to the propeller plane is D . This short length was used to ensure that the non-uniform inflow would not dissipate. The rotating and stationary zones are associated with each other through a mesh interface. The transient rotor-stator model was used to predict the transient flow field around the rotating propeller.

Structured grids were generated for the stationary zone and the hybrid grids were generated for the rotational zone. **Fig. 7** shows the meshes of the rotational zone. The left side of it shows the tetrahedron and hexahedron cells in the rotational zone; the right side of it shows the prism boundary layer mesh near the blades. The thickness of the first layer is 0.8 mm, the thickness of the fourth layer is 1.2 mm. The stationary zone contained about 7.6 million hexahedral cells and the rotational zone contained about 3.4 million tetrahedral/hexahedral cells. It means that the whole computational domain contained about 11 million mixed cells in total. In order to perform the grid sensitivity analysis, a coarse mesh (7.3 million cells) and a fine mesh (16.5 million cells) were also generated.

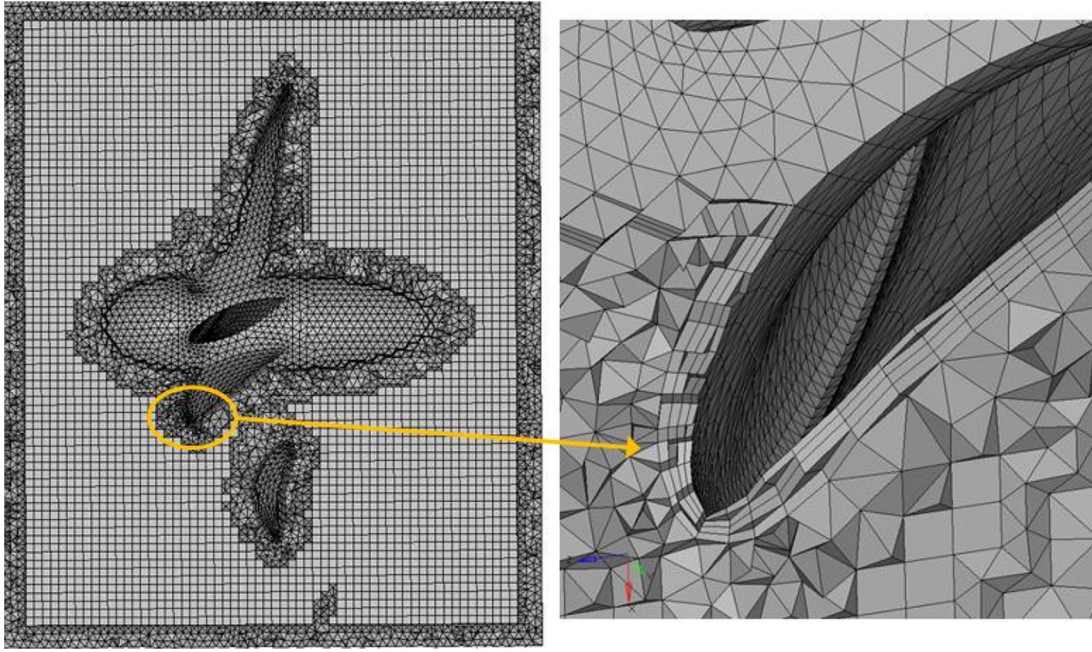


Fig. 7. Meshes of the rotational zone.

A velocity inlet boundary condition was used to define the flow inlet. A pressure outlet was applied for the flow outlet. The no-slip wall was applied to the propeller and the cylinder wall. The central difference scheme was used for the advection equation and the second order backward Euler scheme was used for the transient formulation. A time step of $\Delta t = 10^{-4}$ s was used, which produced a maximum Courant-Frederichs-Levy number of 0.18 for the 11 million cells model.

Transient analysis was performed using three different grid densities at an advance ratio of 0.4. The thrust coefficient $K_T = T/(\rho n^2 D^4)$ was calculated and compared. Fig. 8(a) shows the convergence history of the thrust coefficient of different grid densities; Fig. 8(b) shows the average value of the thrust coefficient between $t = 1$ s and $t = 1.8$ s. It can be seen that with 7.3 M cells we have a result which could be converged for that particular mesh. By increasing the mesh resolution to 11 M cells, there has been an increase in the average thrust coefficient which is not within the defined tolerance (0.005) as shown in Fig. 8(b). By increasing the mesh resolution further, it can be found that 16.5 M cells simulation results in a value that is within the acceptable range. This indicates that we have reached a solution value that is independent of the mesh resolution, and for further analysis we can use the 11 M cells case, as it will give us a result within the defined tolerance.

In order to define the spatially cyclic velocity inlet in CFD simulations, the measured axial velocity distributions were analyzed harmonically. The measured axial velocity V_{ax} at any radius was characterized as follows:

$$V_{ax} = V_0 + \sum_{N=1}^{15} \{ k \cos [N\theta_w - (\text{PHASE})_N] \} \quad (6)$$

where V_0 is the mean axial velocity, θ_w is the angle about the propeller axis, PHASE is the angle of the n^{th} harmonic of axial wake inflow.

This velocity function was applied to the velocity inlet using CFX expression language. In order to compare with the experimental results, the CFD simulations were performed at $J = 0.31$ with 16 different rotational speeds as shown in Table 3. Fig. 9 shows the

axial velocity distribution of the CFD model at $U = 1$ m/s which is calculated from the measured data in Fig. 12 using Eq. (6).

3.2. Flow-induced vibration analysis model

The flow-induced prediction was performed using a combined FEM-BEM approach. FEM was used for the modal analysis in air and BEM was used for the coupled modes calculations and the flow-induced vibration analysis by adopting an indirect formulation[13]. The fundamental governing equations of the coupled modes analyses are given in what follows. The natural frequencies of an uncoupled structure and the associated mode shapes are obtained from the following eigenvalues problem[14]:

$$[\mathbf{K}_s - \omega^2 \mathbf{M}_s] \{\mathbf{u}\} = \{\mathbf{0}\} \quad (7)$$

where the matrices \mathbf{K}_s and \mathbf{M}_s are the stiffness and mass matrices respectively, \mathbf{u} represents the displacement vector. For a fluid-loaded structure the corresponding eigenvalue problem becomes

$$[\mathbf{K}_s - \omega^2 (\mathbf{M}_s + \mathbf{M}_a)] \{\mathbf{u}\} = \{\mathbf{0}\} \quad (8)$$

where \mathbf{M}_a is the added mass matrix representing the effect of the fluid loading on the structure. This added mass matrix is frequency-dependent; hence the complete coupled problem is described by:

$$[\mathbf{K}_s - \omega^2 (\mathbf{M}_s + \mathbf{M}_a(\omega))] \{\mathbf{u}\} = \{\mathbf{0}\} \quad (9)$$

The frequency-dependent problem was approximated by calculating the added mass matrix at a constant frequency ω_0 and extracting the eigenmodes and associated eigenvalues (coupled mode eigenfrequencies) for the following approximate problem:

$$[\mathbf{K}_s - \omega^2 (\mathbf{M}_s + \mathbf{M}_a(\omega_0))] \{\mathbf{u}\} = \{\mathbf{0}\} \quad (10)$$

Different coupled modal bases are obtained for different values of ω_0 , but in practice the difference is small, provided that ω_0 is within the eigenfrequencies range.

The finite element model which included one propeller blade was developed by ANSYS using solid185 and mass21 elements. The mass element was used to simulate the effect of the accelerometer

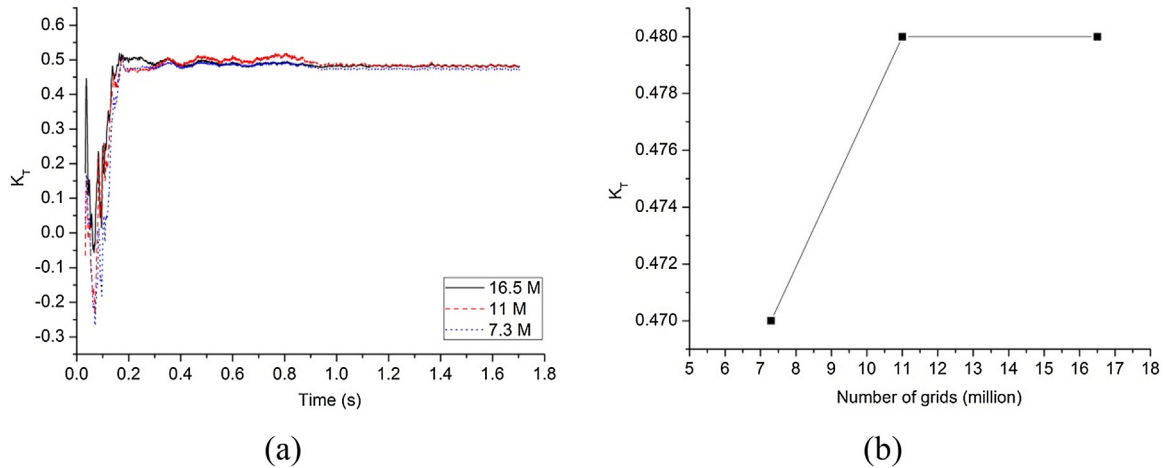


Fig. 8. (a) Convergence history of the thrust coefficient of different grid densities; (b) Average value of the thrust coefficient between $t = 1$ s and $t = 1.8$ s.

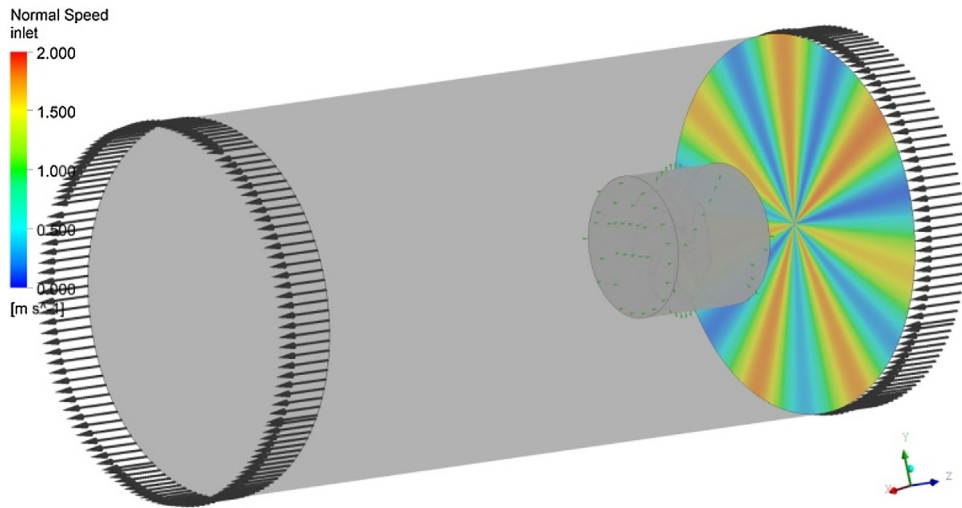


Fig. 9. Axial velocity distribution of the CFD model at $U = 1$ m/s.

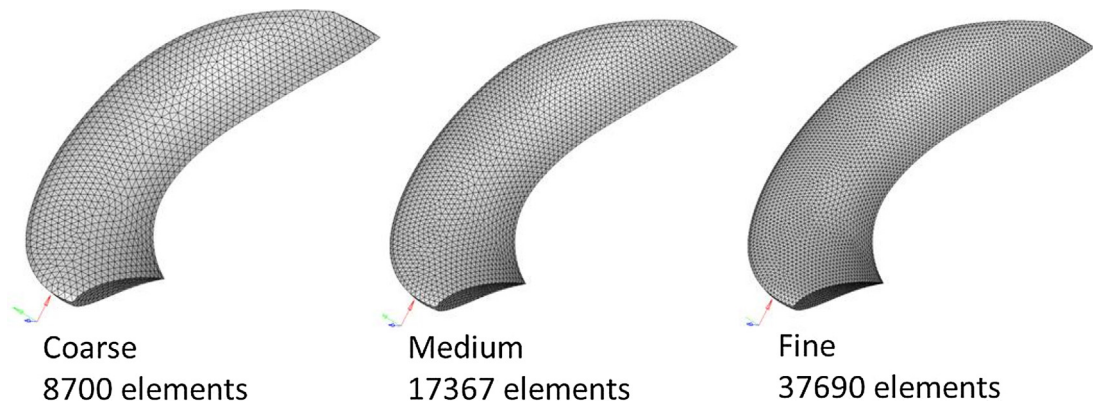


Fig. 10. Three levels of mesh density for the finite element model.

on the blade. Because of the complex geometry of the blade, tetrahedron elements were used in the finite element models. Three levels of mesh density as shown in Fig. 10 were used to investigate the grid sensitivity of the finite element model. The fundamental frequency of the plastic propeller in air was calculated and compared using coarse, medium and fine meshes. Table 4 lists the summary of the grid sensitivity analysis. It can be indicated that the medium mesh which contains 17367 tetrahedron elements, is

suitable for the modal analysis. Two finite element models with medium mesh were developed for the plastic propeller and the bronze propeller for the further analysis.

The calculated modes in air and the wall pressure fluctuations were imposed as the dynamic characteristics and load conditions for the boundary element method analysis respectively. For the modes and load conditions on the boundary element surface, the modal superposition response analysis was performed to calculate

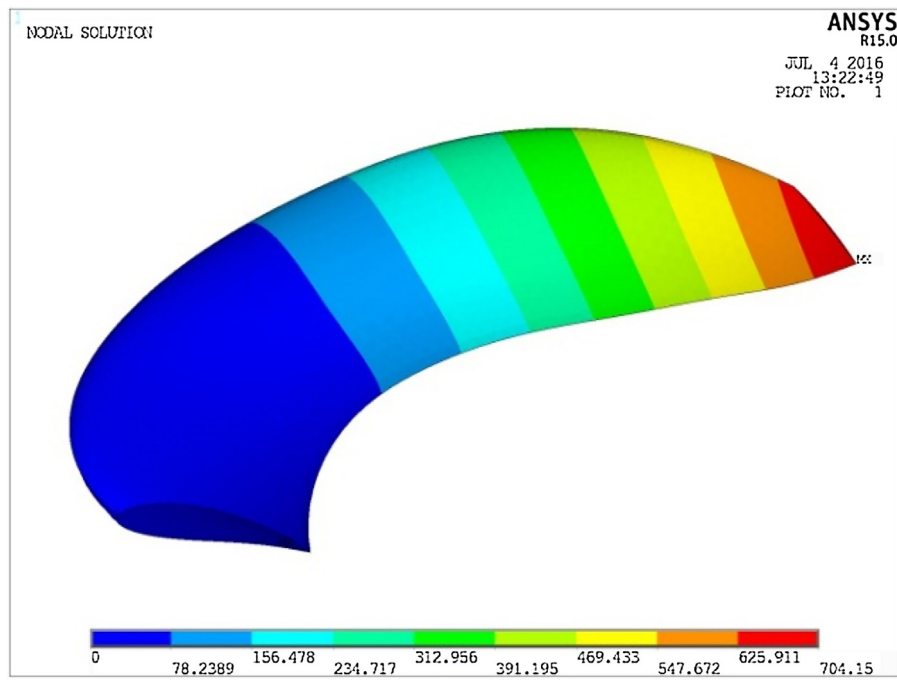


Fig. 11. Fundamental mode shape of the propeller blade.

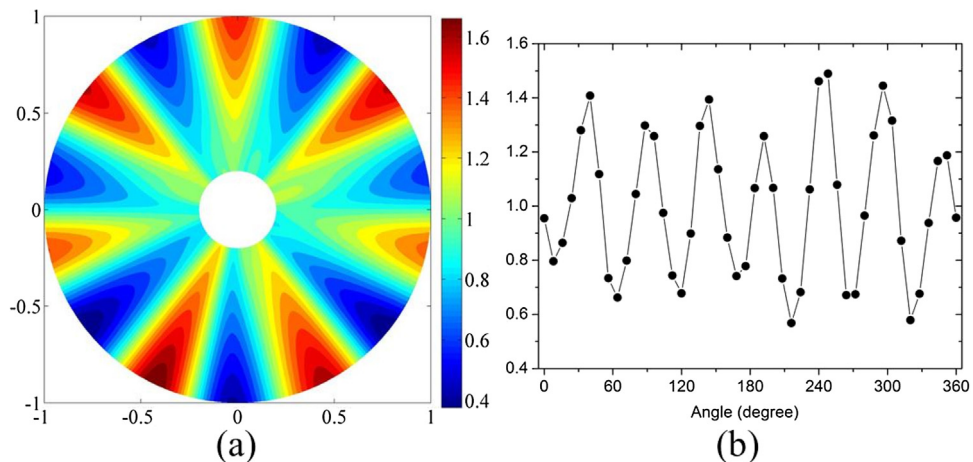


Fig. 12. Measured time-averaged normalized axial velocity (U_{ax}/U) at $U = 1$ m/s. (a) seven-cycle distribution; (b) seven-cycle circumferential distribution at 0.7R.

Table 4
Summary of the grid sensitivity analysis.

	Number of elements	Calculated fundamental frequency (Hz)
Coarse	8700	195.4
Medium	17367	194.9
Fine	37690	194.9

the pressure and normal velocity values at all boundary nodes. A monitor point which has the same location as the accelerometer was used to obtain the vibration response of the blade.

4. Results and discussion

In what follows, results of the propeller mode shapes in air and in water, the pressure fluctuations of the propeller blade, and the vibration response obtained numerically and experimentally are discussed and compared.

4.1. Modal results

The fundamental mode of a propeller is a simple flexural cantilevered mode with its node coincident with the blade root. Fig. 11 illustrate the numerical result of the fundamental mode shape of a single blade. For the propeller-water coupled system, the corresponding coupled mode shapes differ relatively little from mode shapes identified in the uncoupled state. The principal effect of immersing the propeller in water is to cause a reduction in the frequency at which a particular mode of vibration occurs[15]. In the present study, the propellers' fundamental mode shapes in water were considered the same as that in air. Table 5 lists the experimental and numerical results of the two propellers' fundamental frequencies.

4.2. LDV measured axial velocity profile

Fig. 12 shows the normalized axial velocity (U_{ax}/U) at $U = 1$ m/s with the seven-cycle wake screen. U is the tunnel speed measured

Table 5

Fundamental frequencies of the two propellers obtained experimentally and numerically, in air and in water.

	Fundamental frequency in air (Hz)		Fundamental frequency in water (Hz)	
	Experimental	Numerical	Experimental	Numerical
Plastic propeller	195.2	194.9	79.7	79.6
Bronze propeller	519.1	518.9	388.4	388.1

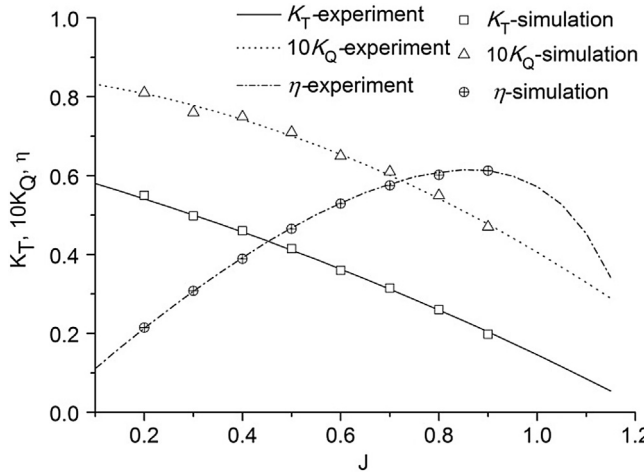


Fig. 13. Open water characteristics of the model propeller.

by the ultrasonic flowmeter. U_{ax} is the measured time-averaged axial velocity. Fig. 12(a) is the normalized axial velocity distribution and Fig. 12(b) is the circumferential velocity profile at 0.7R. The results indicate that the present wake screen technique succeeds in generating the seven-cycle inflow.

The objective of the wake screen was to generate the measurable cyclic wake, which has enough amplitude to excite the propeller vibration. Operating in this kind of cyclic inflow, the propeller blades would experience strong fluctuating forces, which enables distinct vibration signal to be measured by the accelerometer.

4.3. CFD results

In order to validate the present numerical method further, the open water characteristics of the model propeller were calculated. In the case of $J=0.4$, $n=10$, the y plus values on the propeller wall vary from 1 to 6. The corresponding Reynolds number $Re = \frac{\rho n D^4}{\mu}$ is 3.9×10^4 . In the maximum $Re = \frac{\rho n D^4}{\mu} = 5 \times 10^4$ case ($J=0.31$, $n=770/60$), the y plus values on the propeller wall vary from 1.2 to 6.6. Fig. 13 shows the experimental and numerical results of the thrust coefficient $K_T=T/(\rho n^2 D^4)$, the torque coefficient $K_Q=Q/(\rho n^2 D^5)$ and the open water efficiency $\eta=K_J/(2\pi K_Q)$, where T , Q , D , J , n , μ and ρ are the thrust, torque, diameter, advance ratio, rotational speed, dynamic viscosity and the density of the fluid respectively. The results show that the calculated open water characteristics are in good agreement with the experimental values. This indicates that the present numerical model is suitable for predicting the propeller forces. It should be noted that the validation of the CFD model is competent but limited in the paper, for it is not the core of the present paper, which mainly focuses on the flow induced vibration analysis.

Considering the similar flow properties, the CFD results at $J=0.31$ and the rotational speed of 600 rpm were analyzed and discussed. Fig. 14 shows the pressure distributions of the propeller. The pressure on the pressure side is in general higher than that on the suction side. It is this pressure difference of the two sides that produces the thrust. Low pressure region can be found near the blade tip on the suction side. Similarly, high pressure region can be found near the blade tip on the pressure side. Fig. 15 shows the locations of the monitor nodes on the propeller blade. The blade pressure distribution of each time step was recorded to calculate the frequency properties of the blade pressure fluctuations. Fig. 16 shows the time history of the pressure fluctuations during three revolutions (0.3 s). It can be found that the pressures of the four

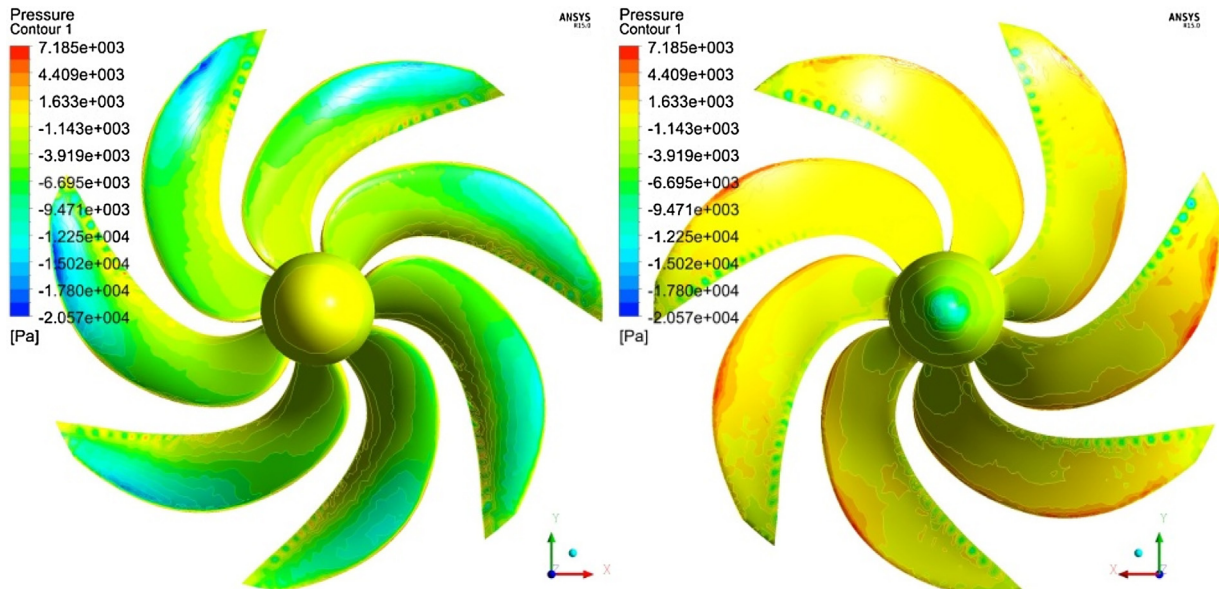


Fig. 14. Pressure distributions of the propeller suction side (left) and pressure side (right).

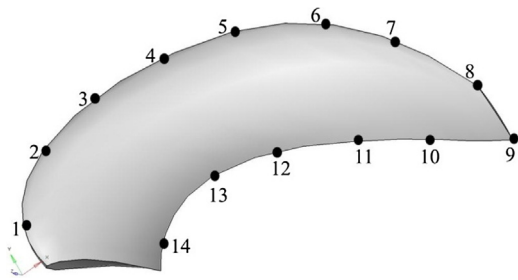


Fig. 15. Locations of the monitor nodes on the propeller blade.

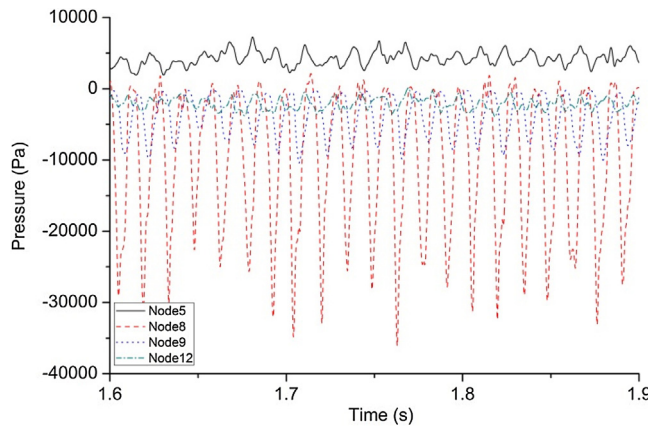


Fig. 16. Time history of the pressure fluctuations during three revolution.

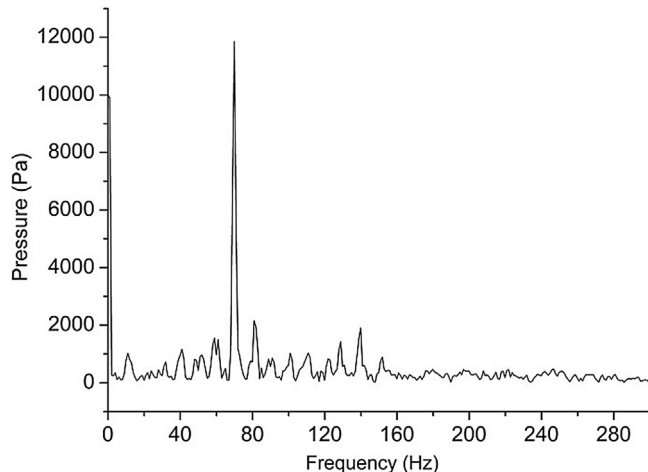


Fig. 17. Pressure frequency spectrum of node 8.

nodes have seven peaks during one revolution (0.1 s) which was induced by the seven-cycle inflow. Compared with the pressures fluctuations on trailing edge, the pressures fluctuations on leading edge are much stronger. There are two reasons why the pressure fluctuations are not strictly periodic: (i) the axial velocity on the inlet as shown in Fig. 12 is not strictly a periodic function; (ii) The unsteady vortex shedding from the blade contributes to the pressure fluctuations.

Node 8 located at the blade tip is observed to have the largest fluctuating amplitude which is induced by the high flow velocity and the strong flow separation near the tip. Fig. 17 shows the pressure frequency spectrum of node 8. As the rotational speed is 600 rpm, the axial passing frequency (APF) is 10 Hz. The spectrum has a high peak at 70 Hz (7APF) which is caused by the seven-cycle inflow. This result is consistent with the time history of the pressure

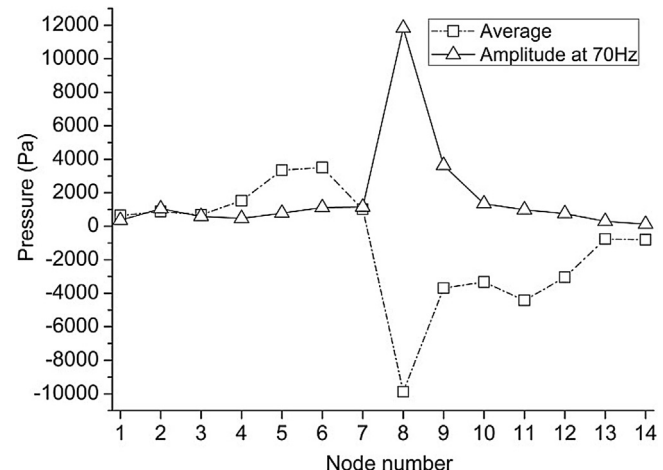


Fig. 18. Time-averaged pressure and the pressure amplitude at 70 Hz of the monitor nodes.

fluctuations as shown in Fig. 16. Fig. 18 shows the time-averaged pressure and the pressure amplitude at 70 Hz of the monitor nodes. It can be seen that the pressure fluctuations near the blade are much stronger than the other regions. Fig. 19 illustrates the blade pressure distributions at different frequencies. The pressure distributions exhibit different patterns at different frequencies. At zero frequency, the pressure distribution is similar as the transient pressure distribution as shown in Fig. 14. At low frequencies, the pressure distributions have distinct high or low pressure regions, while at rather high frequencies (higher than 100 Hz), the pressure distributions trend to be uniform. These high or low pressure regions are mainly caused by the vortex shedding from the blade. At the present rotational speed, the vortex shedding frequency is in general less than 100 Hz. Hence, at rather high frequencies (higher than 100 Hz), the pressure distributions trend to be uniform. These results give us deep insight into the pressure fluctuations on the propeller blade induce by the cyclic inflow.

Fig. 20 shows the time history of the blade normal forces during one revolution. It can be seen that all the forces have seven peaks during one revolution. The z direction force, which has the same direction as the propeller thrust has the largest fluctuating amplitude. The seven strong peaks correspond to the seven heavy loading conditions during a revolution induced by the seven low axial velocity regions as shown in Fig. 12. Fig. 21 shows the frequency spectrum of the z direction force. This frequency spectrum, which has a zero DC component, was calculated using the force data in 1 s corresponding to a frequency resolution of 1 Hz. The spectrum has a strong peak at 70 Hz (7APF), which is consistent with the result in time domain.

4.4. Vibration response results

Experiments were carried out at $J=0$ first to investigate the basic characteristics of the propeller-shaft system. Fig. 22 shows the measured acceleration response spectra at 120 rpm, 240 rpm, 360 rpm and 480 rpm of the plastic propeller, where g is gravitational acceleration. The dominant frequencies are observed to occur at APF and its harmonics. The amplitudes of the peaks at APF are far larger than the amplitudes at its harmonics. These results are in good agreement with Swindenbank's work [16]. The peaks at APF and its harmonics are mainly caused by imbalances of the propeller-shaft system. No matter how well the propeller-shaft system might be balanced, there will always remain some small amount of imbalance or initial curvature, which leads to the response peaks at APF and its harmonics.

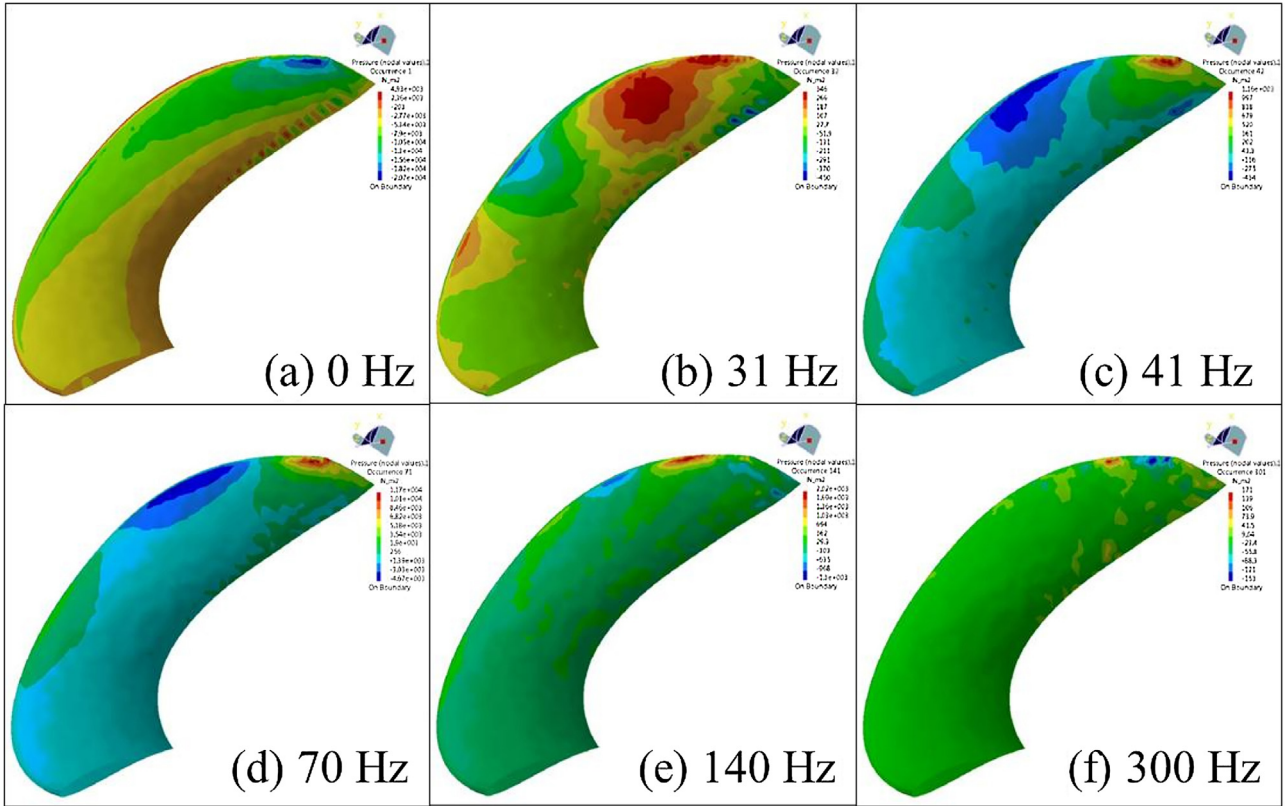


Fig. 19. Blade pressure distributions at different frequencies.

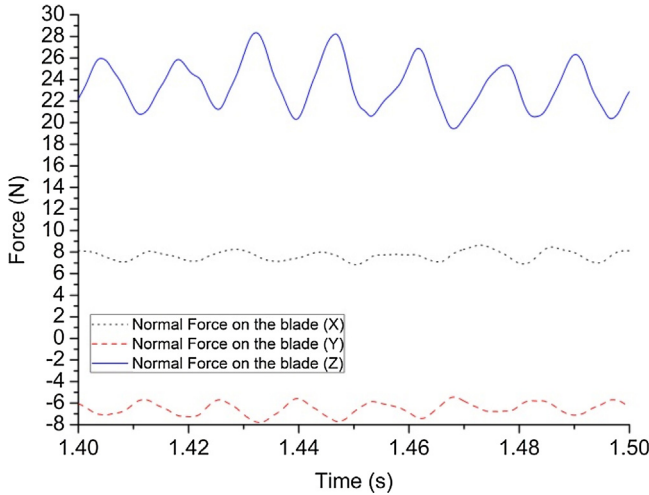


Fig. 20. Time history of the blade normal forces during one revolution.

As shown in Fig. 23, the frequency characteristics of the bronze propeller's acceleration response at $J=0$ are the same as the plastic one, which also show strong peaks at APF. However, compared with the plastic propeller, the amplitudes of the peaks at APF decrease 40%.

Fig. 24 shows the measured acceleration response spectrum of the plastic propeller at $J=0.31$, 600 rpm. The dominant frequencies still occur at APF and its harmonics. The peak at 7APF (70 Hz) has the largest amplitude among the harmonics. These results are noticeably different from the results obtained with a zero tunnel speed. The strong peak at 7APF corresponds to the heavy loading conditions when the propeller blades pass through each of the seven low axial velocity regions as shown in Fig. 12. Fig. 25 shows the

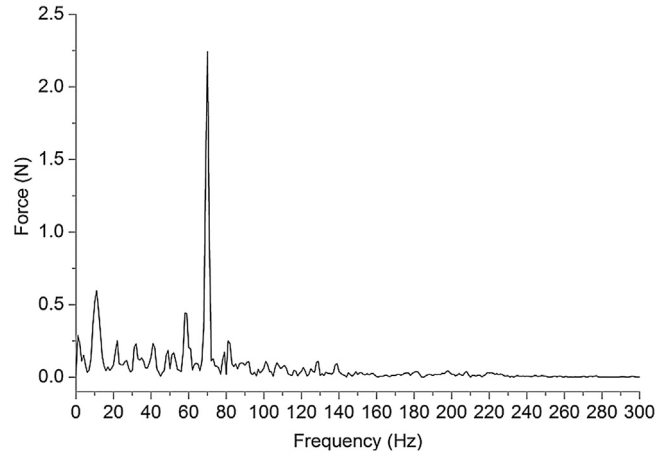
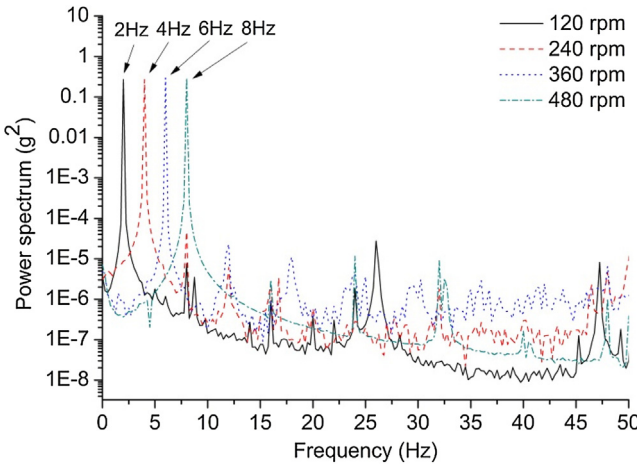
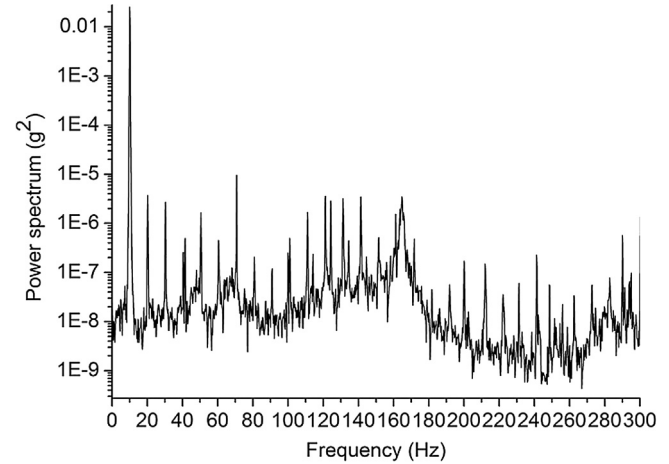
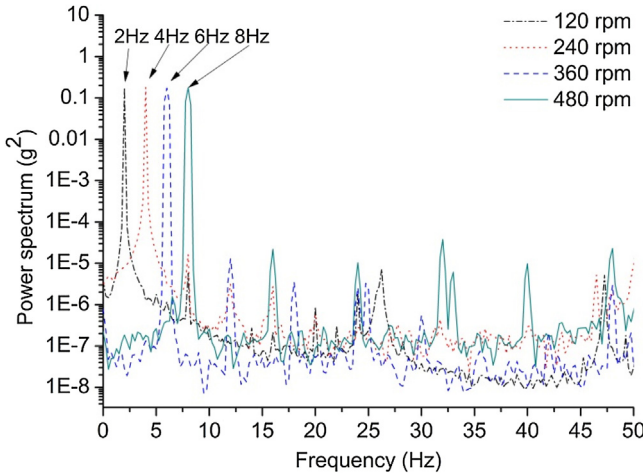
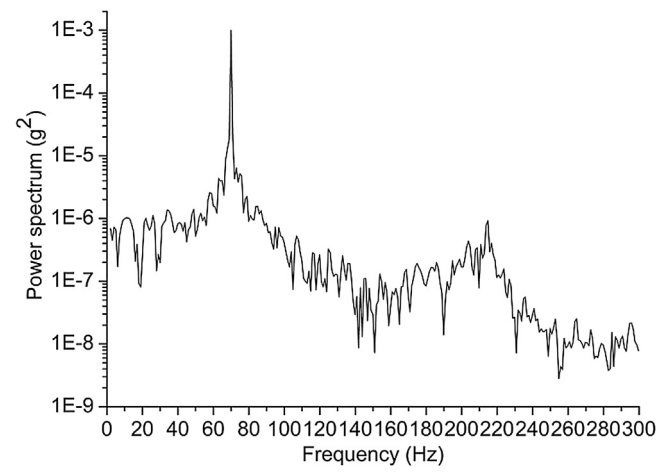
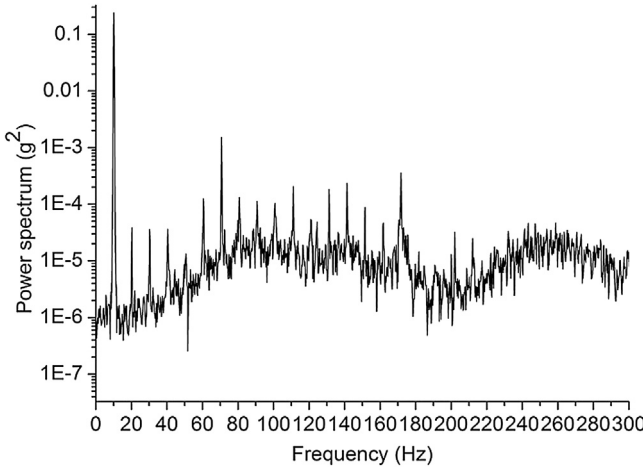


Fig. 21. Z direction force frequency spectrum.

measured acceleration response spectrum of bronze propeller with the same operating condition. Similarly, the dominant frequencies occur at APF and its harmonics and the peak at 7APF (70 Hz) has the largest amplitude. However, the amplitude of the plastic propeller's power spectrum at 7APF is about 1000 times as large as the amplitude of the bronze propeller's power spectrum at 7APF. The stiffness of the propeller is found to have a great effect on the vibration response.

Fig. 26 shows the numerical result of the acceleration response spectrum of the plastic propeller at $J=0.31$, 600 rpm. The strong peak at 7APF is consistent with the experimental result. This indicates that the present numerical method succeeds in predicting the vibration response induced by the seven-cycle inflow. However, the numerical acceleration response does not have distinct peaks

Fig. 22. Measured acceleration response at $J=0$, plastic propeller.Fig. 25. Measured acceleration response at $J=0.31$, 600 rpm, bronze propeller.Fig. 23. Measured acceleration response at $J=0$, metal propeller.Fig. 26. Numerical results of acceleration response at $J=0.31$, 600 rpm, plastic propeller.Fig. 24. Measured acceleration response at $J=0.31$, 600 rpm, plastic propeller.

at APF and its other harmonics which is different from the experimental results. This is because that the numerical model is not able to consider the imbalances of the real propeller-system. Hence, the peaks at APF and its harmonics disappear except 7APF, which is the caused by the forced vibration excited by the seven-cycle inflow.

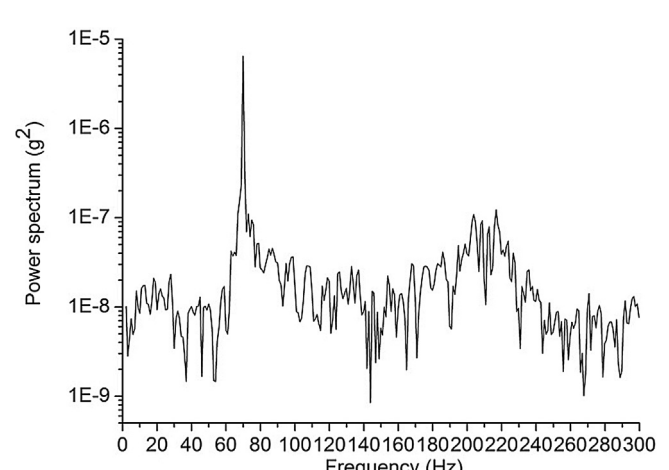
Fig. 27. Numerical results of acceleration response at $J=0.31$, 600 rpm, bronze propeller.

Fig. 27 shows the numerical result of the acceleration response spectrum of the bronze propeller at $J=0.31$, 600 rpm. Similarly, the strong peak at 7APF is observed.

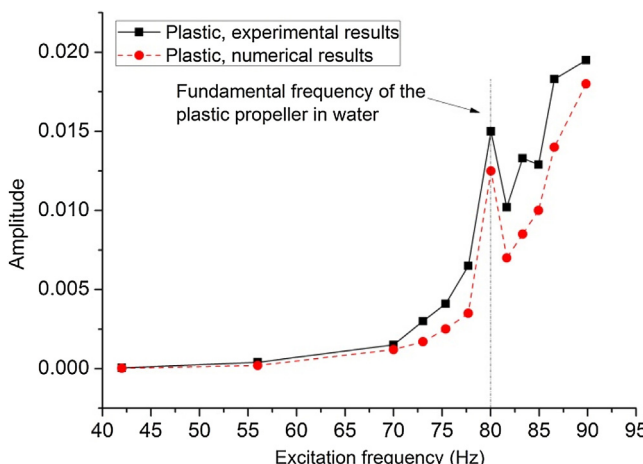


Fig. 28. Measured and calculated vibration response as a function of the 7APF excitation frequency, plastic propeller.

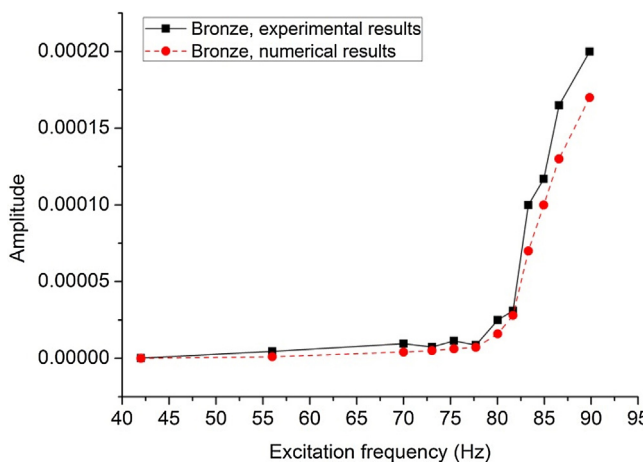


Fig. 29. Measured and calculated vibration response as a function of the 7APF excitation frequency, bronze propeller.

4.5. Vibration near the propeller's fundamental frequency

As discussed in Table 5, the fundamental frequencies of the plastic and bronze propellers in water are 79.6 Hz and 388.1 Hz, respectively. The two propellers were operated over a series of shaft rotational speeds up to 770 rpm with the seven-cycle inflow, which produced a 7APF excitation frequency up to 89.8 Hz. The excitation frequencies span the plastic propeller's fundamental frequency, while are far from the bronze propeller's fundamental frequency.

Fig. 28 shows the measured and calculated power spectra amplitude at 7APF as a function of the 7APF excitation frequency of the plastic propeller. The response curve has a peak at 80 Hz, which corresponds to the plastic propeller's fundamental frequency. This indicates that the resonance occurred when the 7APF excitation frequency coincided with the propeller's fundamental frequency. This behavior can be explained by the force amplification effect induced by the blade vibrating at the resonant frequency. The variation of the calculated response is found to be consistent with the measured results. The results also indicate that the present numerical method can be used to predict the forced vibration excited by the seven-cycle inflow with reasonable accuracy.

Fig. 29 shows the measured and calculated power spectra amplitude at 7APF as a function of 7APF excitation frequency of the bronze propeller. The response amplitudes increase with the exci-

tation frequency, which is different from the response curve of the plastic propeller.

In some cases, the repeated measurements were performed with the same water tunnel setting. The results showed that the mean acceleration values agreed to within 4% which indicated that the measurements were reliable.

5. Conclusion

A comprehensive study of the flow-induced vibration of propellers operating in the non-uniform inflow which the phase of incoming flow perturbations is taken into account has been conducted. The LDV measured axial velocity distributions show that the present wake screen technique succeeded in generating the seven-cycle inflow which had enough amplitude to excite the propeller vibration.

When the propeller was operating with a zero tunnel speed, the dominant frequencies of the measured acceleration response spectra occur at APF and its harmonics; When the propeller was operating at $J=0.31$, the dominant frequencies of the measured acceleration response spectra still occur at APF and its harmonics. However, the peak at 7APF has the largest amplitude among the harmonics which are noticeably different from the results obtained with a zero tunnel speed. The strong peak at 7APF corresponds to the heavy loading conditions when the propeller blades pass through each of the seven low axial velocity regions as shown in Fig. 12.

The response curve of the plastic propeller, which presents the power spectra amplitude at 7APF as a function of the 7APF excitation frequency, has a peak at 80 Hz, which corresponds to the plastic propeller's fundamental frequency. This demonstrates that the resonance occurred when the 7APF excitation frequency coincided with the plastic propeller's fundamental frequency. This behavior can be explained by the force amplification effect induced by the blade vibrating at the resonant frequency. However, this response curve of the bronze propeller increases with the excitation frequency, which is different from that of the plastic propeller.

In numerical simulations, the measured axial velocity was applied to the velocity inlet using CFX expression language in the format of Eq. (6). The results are in general agreement with the experimental results. The present numerical method can be used to predict the forced vibration response induced by the seven-cycle inflow. However, the numerical model is not able to consider the imbalances of the real propeller-system. Hence, the peaks at APF and its harmonics disappear except 7APF, which is caused by the forced vibration excited by the seven-cycle inflow.

References

- [1] S. Merz, R. Kinns, N. Kessissoglou, Structural and acoustic responses of a submarine hull due to propeller forces, *J. Sound Vib.* 325 (2009) 266–286.
- [2] J.E. Brooks, Vibrations of a marine propeller operating in a nonuniform inflow. DAVID W TAYLOR NAVAL SHIP RESEARCH AND DEVELOPMENT CENTER BETHESSDA MD, 1980.
- [3] S. Javdani, M. Fabian, J.S. Carlton, T. Sun, K.T. Grattan, Underwater free-vibration analysis of full-scale marine propeller using a fiber bragg grating-based sensor system, *IEEE Sens. J.* 16 (2016) 946–953.
- [4] M. Seaver, S.T. Trickey, J.M. Nichols, Strain measurements from FBGs embedded in rotating composite propeller blades, *Optical Fiber Sensors: Optical Society of America* (2006) (p. ThD2).
- [5] F. Dreier, P.G. x00Fc, T. nther Pfister, J.W. Czarske, et al., Interferometric sensor system for blade vibration measurements in turbomachine applications, *IEEE Trans. Instrum. Meas.* 62 (2013) 2297–2302.
- [6] B. Gwashavanh, A.J. Oberholster, P.S. Heyns, Rotating blade vibration analysis using photogrammetry and tracking laser Doppler vibrometry, *Mech. Syst. Sig. Process.* 76 (2016) 174–186.
- [7] P.L. Mikrut, S.C. Morris, J.D. Cameron, Compressor blade vibration measurements using blade image velocimetry, *J. Vib. Acoust.* 137 (2015) 061007.
- [8] H.J. Lin, J.F. Tsai, Analysis of underwater free vibrations of a composite propeller blade, *J. Reinf. Plast. Compos.* 27 (2008) 447–458.

- [9] A. Ducoin, Y.L. Young, Hydroelastic response and stability of a hydrofoil in viscous flow, *J. Fluids Struct.* 38 (2013) 40–57.
- [10] Y. Wei, Y. Wang, Unsteady hydrodynamics of blade forces and acoustic responses of a model scaled submarine excited by propeller's thrust and side-forces, *J. Sound Vib.* 332 (2013) 2038–2056.
- [11] S.D. Jessup, Measurement of Multiple Blade Rate Unsteady Propeller Forces, DTIC Document, 1990.
- [12] P. Sagaut, Large Eddy Simulation for Incompressible Flows: an Introduction, Springer Science & Business Media, 2006.
- [13] R. Citarella, L. Federico, A. Cicatiello, Modal acoustic transfer vector approach in a FEM-BEM vibro-acoustic analysis, *Eng. Anal. Boundary Elem.* 31 (2007) 248–258.
- [14] O. von Estorff, *Boundary Elements in Acoustics: Advances and Applications*: Wit Pr/Computational Mechanics, 2000.
- [15] F.J. Fahy, P. Gardonio, *Sound and Structural Vibration: Radiation, Transmission and Response*, Academic press, 2007.
- [16] S.B. Switzenbank, S. Jessup, A. Etebari, Measurement of Crashback Loads on a Blade of Propeller 4381 in an Open and Ducted Configuration in the 36-inch Water Tunnel, DTIC Document, 2008.